
Comparative RANS turbulence modelling of lost salt core viability in high pressure die casting

Sebastian Kohlstädt* and Michael Vynnycky

Department of Materials Science and Engineering,
KTH Royal Institute of Technology,
Brinellvägen 23,
100 44 Stockholm, Sweden
Email: skoh@kth.se
Email: michaelv@kth.se
*Corresponding author

Alexander Neubauer and Andreas Gebauer-Teichmann

Volkswagen AG – Division of Components Manufacturing,
Business Unit Casting,
Dr. Rudolf-Leiding-Platz 1,
34225 Baunatal, Germany
Email: neubauer.alexander@gmx.net
Email: andreas.gebauer-teichmann@volkswagen.de

Abstract: In this work, the implementation of three turbulence models inside the open source C++ computational fluid dynamics (CFD) library OpenFOAM were tested in 2D and 3D to determine the viability of salt cores in high pressure die casting. A finite-volume and volume of fluid approach was used to model the two-phase flow of molten metal and air, with the latter being treated as compressible. Encouragingly, it is found that, although the choice of turbulence model seems to affect the dispersion of the two-phase interface, the force acting at the surface of the salt core depends only very weakly on the turbulence model used. The results were also compared against those obtained using the commercially available and widely-used casting software MAGMA⁵.

Keywords: turbulence; RANS; volume-of-fluid method; OpenFOAM; high pressure die casting; HPDC; aluminium; lost cores; salt core viability.

Reference to this paper should be made as follows: Kohlstädt, S., Vynnycky, M., Neubauer, A. and Gebauer-Teichmann, A. (2019) ‘Comparative RANS turbulence modelling of lost salt core viability in high pressure die casting’, *Progress in Computational Fluid Dynamics*, Vol. 19, No. 5, pp.316–327.

Biographical notes: Sebastian Kohlstädt is a graduate from the KTH Royal Institute of Technology in Stockholm, Sweden. He is currently an R&D Engineer at Volkswagen in Kassel, Germany, as well as an industrial PhD student at KTH.

Michael Vynnycky is currently the Head of the Casting of Metals research group at KTH Royal Institute of Technology in Stockholm, Sweden. He holds a PhD in Applied Mathematics from Oxford University and has previously held academic posts in Japan, Ireland and Brazil.

Alexander Neubauer is a graduate of Brunswick Technical University and University of Applied Sciences and Arts Hildesheim/Holzminden/GoettingenGermany, and currently a Masters student at the Volkswagen Kassel plant.

Andreas Gebauer-Teichmann holds a PhD from Brunswick Technical University, Germany and is currently the Volkswagen Casting research group leader. He previously led research groups at Fraunhofer Gesellschaft.

1 Introduction

High pressure die casting (HPDC) is an important process for manufacturing high volume and low cost automotive components, such as automatic transmission housings and

gear box components. Liquid metal, generally aluminium, is injected through complex gate and runner systems and into the die at high speed, typically between 50 and 100 ms⁻¹, and under very high pressures. However, it has up to date

proven difficult to employ lost cores within the process. The basic idea of using salt cores is to create undercuts or hollow sections with them, which may then later act as cooling or oilflow channels. Given this process constraint in design freedom for the CAD-engineer, the idea of using salt as the material for lost cores has been put forward by machine manufacturers, as well as automotive companies (Jelínek and Adámková, 2014). One way to determine whether this is indeed viable is to employ numerical simulation.

However, such studies are certainly far from exhaustive. The only examples of core viability simulation that we have been able to find are those due to Fuchs et al. (2013) and Fuchs and Körner (2014), who employed the commercial computational fluid dynamics (CFD) software Flow-3D, in order to compute the nonisothermal, turbulent, multiphase (molten metal/air) flow that occurs. In both cases, RANS (Reynolds Averaged Navier Stokes) modelling was adopted to take account of the turbulence, via the use of the Renormalised Group (RNG) $k-\varepsilon$ model (Yakhot et al., 1992). The RNG model is considered to be a more robust version of the two-equation $k-\varepsilon$ model (Lauder and Spalding, 1974), and is recommended for most industrial problems. It extends the capabilities of the standard $k-\varepsilon$ model to provide better coverage of transitionally turbulent flows, curving flows, wall heat transfer, and mass transfer.

In this context, the purpose of this paper is twofold. The first will be to examine whether the choice of RANS turbulence model affects the stress on the salt core, and hence its viability. The second is to commence to move away from the use of commercial software and towards the development of open source software for HPDC modelling. To achieve these goals, we use the open-source C++ CFD library OpenFOAM (Weller et al., 1998; Jasak et al., 2007) and employ the $k-\varepsilon$, $k-\omega$ -SST (shear stress transport) (Menter, 1994) and Spalart-Allmaras turbulence models (Spalart and Allmaras, 1994), together with the volume of fluid (VOF) method (Hirt and Nichols, 1981) to take account of the multiphase flow. We have chosen these three models because they are the ones most often used for turbulent engineering computations. The simplest of these is the Spalart-Allmaras model, which is a so-called one-equation model which solves a transport equation for a viscosity-like variable that is often referred to as the Spalart-Allmaras variable. On the other hand, the $k-\varepsilon$ model is a two-equation eddy-viscosity model which solves transport equations for the turbulent kinetic energy, k and the dissipation ε . As for the $k-\omega$ SST model, it is also a two-equation model, although it solves transport equations for k and the specific dissipation rate, ω ; however, unlike its predecessor, the $k-\omega$ model, it solves for k and ω in nearwall regions, but for k and ε in the free stream away from wall regions. The performance of the three models is compared for a two-dimensional flow containing a core, as given in Figure 1, and then the $k-\omega$ -SST model is used for 3D computations for the flow in the geometry shown in Figures 2 and 3; for the latter case, the results are compared with

those obtained using the commercial casting software MAGMA⁵.

Figure 1 Simplified representation of the two-dimensional model used for the comparison of the turbulence models.

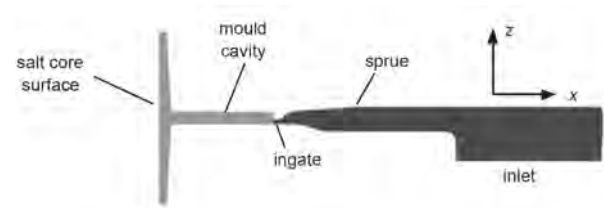
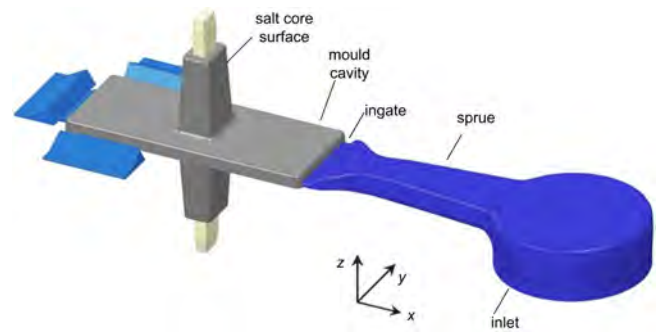
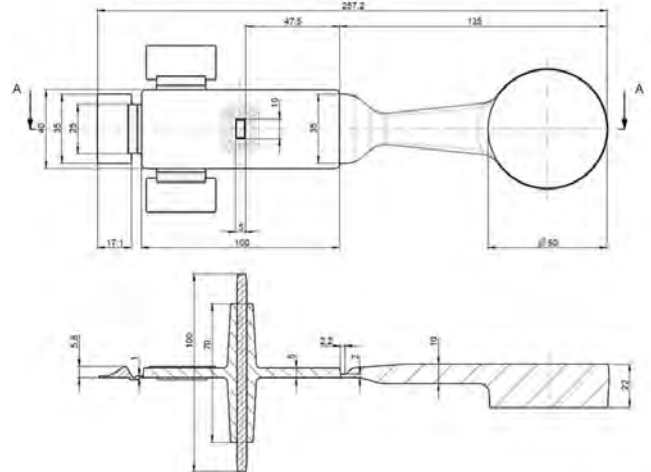


Figure 2 CAD model of the sample geometry in 3D (see online version for colours)



Note: The casting chamber is not illustrated.

Figure 3 Relevant dimensions of the CAD model (in mms)



2 Model equations and simulation method

2.1 Model equations

We model the two-phase flow of molten metal and air in HPDC by using the VOF method, wherein a transport equation for the VOF function, γ , of each phase is solved simultaneously with a single set of continuity and Navier-Stokes equations for the whole flow field; note also that γ , which is advected by the fluids, can thus be interpreted as the liquid fraction. Considering the molten melt and the air as Newtonian, compressible and immiscible fluids, the

governing equations can be written as (Ferrer et al. 2016; Mayon et al., 2016)

$$\frac{\partial \rho}{\partial t} + \nabla \cdot (\rho \mathbf{U}) = 0 \quad (1)$$

$$\begin{aligned} \frac{\partial}{\partial t}(\rho \mathbf{U}) + \nabla \cdot (\rho \mathbf{U} \mathbf{U}) = -\nabla p \\ + \nabla \cdot \{(\mu + \mu_{tur})(\nabla \mathbf{U} + (\nabla \mathbf{U})^T)\} + \rho \mathbf{g} + \mathbf{F}_s \end{aligned} \quad (2)$$

$$\frac{\partial \gamma}{\partial t} + \nabla \cdot (\gamma \mathbf{U}) + \nabla \cdot (\gamma(1-\gamma) \mathbf{U}_r) = -\frac{\gamma}{\rho_g} \left(\frac{\partial \rho_g}{\partial t} + \mathbf{U} \cdot \nabla \rho_g \right) \quad (3)$$

where t is the time, \mathbf{U} the mean fluid velocity, p the pressure, \mathbf{g} the gravity vector, \mathbf{F}_s the volumetric representation of the surface tension force and T denotes the transpose. In particular, \mathbf{F}_s is modelled as a volumetric force by the continuum surface force (CSF) method (Brackbill et al., 1992). It is only active in the interfacial region and formulated as $\mathbf{F}_s = \sigma \kappa \nabla \gamma$, where σ is the interfacial tension and $\kappa = \nabla \cdot (\nabla \gamma / |\nabla \gamma|)$ is the curvature of the interface. The significance of the term \mathbf{U}_r is explained shortly. The material properties ρ and μ are the density and the dynamic viscosity, respectively, and are given by

$$\rho = \gamma \rho_l + (1-\gamma) \rho_g \quad (4)$$

$$\mu = \gamma \mu_l + (1-\gamma) \mu_g \quad (5)$$

where the subscripts g and l denote the gas and liquid phases, respectively. We take ρ_l , μ_g and μ_l to be constant, but use the ideal gas law for ρ_g , so that

$$\rho_g = \frac{\rho M}{RT} \quad (6)$$

where R is the universal gas constant, T is the temperature and M is the gas relative molecular weight. Furthermore, μ_{tur} in equation (2) denotes the turbulent eddy viscosity, which will be calculated via three different turbulence models; the details of these – k - ϵ , k - ω -SST and Spalart-Allmaras – are given in Launder and Spalding (1974), Menter (1994) and Spalart and Allmaras (1994), respectively.

In addition, the heat equation is (Ferrer et al., 2016; Mayon et al., 2016)

$$\begin{aligned} \frac{\partial}{\partial t}(\rho T) + \nabla \cdot (\rho T \mathbf{U}) = \nabla \cdot (\alpha_{eff} \nabla T) \\ - \left(\frac{\gamma}{c_{vl}} + \frac{1-\gamma}{c_{vg}} \right) \left(\nabla \cdot (\rho \mathbf{U}) + \frac{\partial(\rho K)}{\partial t} + \nabla \cdot (\rho K \mathbf{U}) \right) \end{aligned} \quad (7)$$

where $K = \frac{1}{2} \mathbf{U} \cdot \mathbf{U}$ is the kinetic energy, c_{vg} and c_{vl} denote the specific heat capacities at constant volume for the gas and liquid phases, respectively, α_{eff} is given by

$$\alpha_{eff} = \frac{\gamma k_l}{c_{vl}} + \frac{(1-\gamma) k_g}{c_{vg}} + \frac{\mu_{tur}}{\sigma_{tur}}$$

where k_g and k_l denote the thermal conductivities for the gas and liquid phases, respectively, and σ_{tur} is the turbulent Prandtl number, whose value is set to 0.9 (Versteeg and Malalasekera, 2007). Note that α_{eff} resembles a phase-averaged thermal diffusivity that includes the contribution of turbulence, although it lacks a density term in the denominator.

Equations (1)–(7) require boundary conditions. In the HPDC situation under consideration, there are essentially two types of boundaries: an inlet and a wall. At the former, the normal velocity, the temperature and the liquid fraction are prescribed; thus,

$$\mathbf{U} \cdot \mathbf{n}_l = v_l \quad (8)$$

$$T = T_l \quad (9)$$

$$\gamma = 1 \quad (10)$$

where v_l and T_l denote the inlet velocity and temperature, respectively, and \mathbf{n}_l denotes the inward unit normal vector at the inlet. Furthermore, it is necessary to set conditions for the turbulence quantities relevant to each turbulence model. This is done via the turbulence intensity and length scale for the largest eddies, which were set at 5% and 2 mm, respectively. At walls, the tangential and normal components of velocity are zero. In addition, conditions are required for the temperature; for simplicity, we assume that all walls are thermally insulating, so that

$$\nabla T \cdot \mathbf{n}_w = 0 \quad (11)$$

where \mathbf{n}_w denotes the inward unit normal vector at a wall. Note that, whilst the wall boundary conditions for the velocity are standard, they are implemented via wall functions in slightly different ways, according to the turbulence model used. We omit the details here, which can instead be found in Launder and Spalding (1974), Menter (1994) and Spalart and Allmaras (1994).

Lastly, we also require initial conditions. We assume that the cavity initially contains only gas which is stationary and at room temperature, T_0 . Thus, we set

$$\mathbf{U} = 0 \quad (12)$$

$$T = T_0 \quad (13)$$

$$\gamma = 0 \quad (14)$$

The model parameters are given in Table 1; note that it is usually c_{pg} and c_{pl} , the specific heat capacities at constant pressure, that are tabulated, rather than c_{vg} and c_{vl} . However, for air, the value of the isentropic expansion factor or heat capacity ratio, c_{pg} / c_{vg} , can be assumed to be constant and equal to 1.4 for air in the given temperature range (Koch et al., 2016; White, 2011) with acceptable accuracy. On the other hand, the aluminium melt was treated as incompressible in this model; thus, $c_{vl} = c_{pl}$.

Table 1 Model parameters

c_{v_g}	720 Jkg ⁻¹ K ⁻¹
c_{v_l}	1,000 Jkg ⁻¹ K ⁻¹
k_g	0.026 Wm ⁻¹ K ⁻¹
k_l	70 Wm ⁻¹ K ⁻¹
M	0.028 kgmol ⁻¹
T_0	293 K
T_l	823 K
v_l	0.5–1.5 ms ⁻¹
μ_g	1.8 × 10 ⁻⁵ Pas
μ_l	1.62 × 10 ⁻³ Pas
ρ_l	2,520 kgm ⁻³
σ	0.629 Nm ⁻¹

Notes: The parameters for gas are those for air; those for metal are for the alloy AlSi₉Cu₃.

2.2 Simulation method

To solve the above equations, the OpenFOAM environment was used (Weller et al., 1998; Jasak et al., 2007). In general, this is an open-source C++ library for solving partial differential equations mainly for fluid mechanics applications using the finite-volume method (FVM); for details of the latter, see Versteeg and Malalasekera (2007). In particular, we used the *compressibleInterFoam* solver, which handles two compressible, non-isothermal immiscible fluids using a VOF interface-capturing approach. The basic idea is that each volume cell is assigned a value of γ and the physical quantities in that cell are given by equations (4) and (5). These values are then used for solving the discretised Navier-Stokes equations, with the value of γ for each cell being updated iteratively. The solver also uses the multi-dimensional universal limiter with explicit solution (MULES) scheme for interface compression, which introduces a supplementary velocity field, U_r , in the vicinity of the interface. In doing so, the local flow steepens the gradient and the interface becomes sharper and more pristine. A typical form for U_r is $U_r = \min(U, \max(U))$, as given by Ferrer et al. (2016).

For all the simulations, the Courant number (Courant et al., 1967) was chosen to be below 0.8 in the 2D simulations and 0.4 for the 3D simulations. These values were chosen as no increase in accuracy was observed for smaller Courant numbers.

3 Results and discussion

In this section, the modelled form filling and metal flow, as well as the forces acting on the salt core, are visualised, evaluated and discussed. First, in Section 3.1, the influence of different flow velocities and numerical boundary conditions (turbulence model, time step size, mesh resolution) on the simulation result is investigated for a 2D geometry. Then, in Section 3.2, a 3D mould fill simulation is performed with the aid of the commercially available

software MAGMA⁵ and compared with the simulation results of OpenFOAM. These computations were done on the CAD geometry shown in Figure 2. The necessary length dimensions of the CAD-model are also provided in the corresponding engineering drawing in Figure 3.

3.1 2D modelling: Influence of turbulence models

In this section, two-dimensional simulations employing the k - ϵ , k - ω -SST and Spalart-Allmaras turbulence models as implemented in OpenFOAM were conducted. The aim was to identify a suitable turbulence model for the mould filling simulation, taking into account the computation time for the numerical solution and the force profile at the surface of the salt core. For economical reasons, the 3D-geometry shown in Figure 2 was simplified and sliced into a simple representative 2D-geometry, thus drastically reducing the size of the computational grid required; the simplified shape of the model is depicted in Figure 1.

For the computations, a variety of structured meshes having 4,460 to 71,360 cells were tried, but mesh independence with respect to the force on the core was found to be attained for a mesh having 36,708 cells with edge lengths of 0.2–0.5 mm; the results presented later are for this mesh. A constant melt speed at the inlet of $v_l = 1.5 \text{ ms}^{-1}$ was employed. Also, with this mesh, the y^+ -values obtained at walls varied between 30 and 35, with an average of around 35, as is required for all three turbulence models. Moreover, all computations were carried out on a workstation with a hexa-core processor of 12 threads (3.0 GHz) and a total of 32 GB random access memory (RAM).

3.1.1 Flow and metal stream behaviour

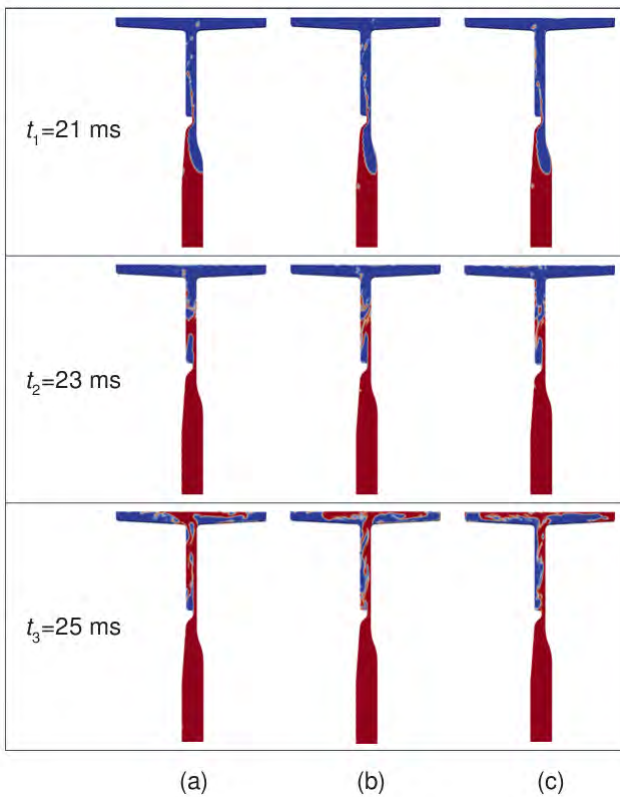
For the analysis of the metal flow profiles as a function of the selected turbulence models, video recordings of the three simulated filling operations were made. Snapshots were created at the times $t_1 = 21 \text{ ms}$, $t_2 = 23 \text{ ms}$ and $t_3 = 25 \text{ ms}$; these are shown in Figure 4.

For all three cases, the flow behaviour observed is typical of die casting when the melt enters the mould cavity region. Thus, as the liquid metal enters into the mould cavity, a splitting of the metal jet is detected, as seen for times t_1 and t_2 . This jet behaviour is characteristic of the die-casting process, and of the high flow velocity and the associated aerodynamic forces. A slightly larger atomisation effect was observed for the k - ϵ and k - ω -SST turbulence models than for the Spalart-Allmaras turbulence model. However, neither this sputtering nor the flow in areas away from the wall gives any accurate assessment of the better or worse suitability of any one of the turbulence models for solving the present flow problem. Unsurprisingly, each model gives different flow patterns during the entire mould filling, since each calculates the turbulent viscosity slightly differently.

In areas close to the wall, flow characteristics typical of the respective turbulence models could be observed. A significant difference between the k - ϵ model, on the one

hand, and the $k-\omega$ -SST and Spalart-Allmaras models on the other, can be seen. When using the $k-\omega$ -SST and Spalart-Allmaras models, a metal film is formed in the flow direction before the gate wall; see Figure 4 for $t = t_1$ (right wall area). When using the $k-\varepsilon$ model, the metal film is not present. Because the resolution of the metal film is an indication of a more accurate modelling of the flow in the vicinity of the wall, the $k-\varepsilon$ model appears to be at a disadvantage by comparison with the other two models. This is also well in line with RANS modelling research publications that observed the $k-\varepsilon$ model to have inferior performance in near-wall regions (Menter, 1994; Wilcox, 1988).

Figure 4 Comparison of the flow when using different turbulence models: (a) $k-\varepsilon$ (b) $k-\omega$ -SST (c) Spalart-Allmaras (see online version for colours)



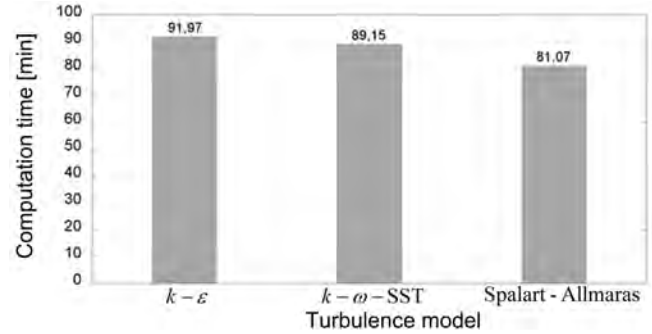
Notes: Red areas characterise the melt, blue areas the air and the mixed colours (white/orange) regions are the interface between melt and air.

3.1.2 Computation time comparison

It is instructive to compare the computing times required using the various turbulence models. This was done by carrying out 2D mould-filling simulations on a core having one processor; the results are shown in Figure 5. As can be seen in Figure 5, the computation times with the $k-\varepsilon$, $k-\omega$ -SST and Spalart-Allmaras models were 92, 89 and 81 minutes, respectively. One of the reasons for the shorter solution time for the Spalart-Allmaras model is that it is a one-equation model; solving one partial differential equation takes less computing time than solving two, as in

the case of the $k-\varepsilon$ and $k-\omega$ -SST models. The results of these comparison study are therefore well in line with algebraic reasoning.

Figure 5 Comparison of the required computation time when using different turbulence models



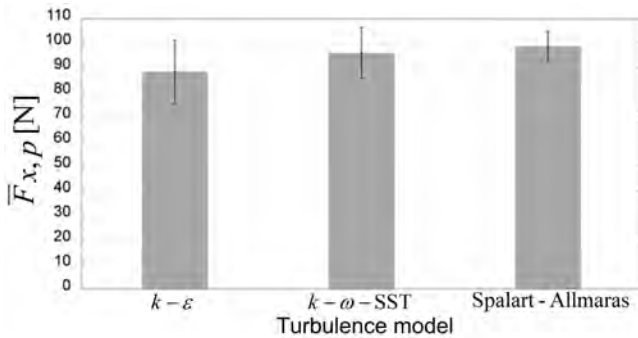
3.1.3 Forces acting on the core

Due to turbulence model-specific eddy viscosity calculation, the acting force on the salt core can differ. For this reason, the influence of the turbulence models on the salt core forces was investigated in more detail. The resulting force differences were determined in the following way. An outlet was constructed on the geometry model, via which the melt could flow out during the filling of the mould; this was placed adjacent and perpendicular to the core surface, and the flow was then computed for this configuration for each of the turbulence models. In the absence of the outlet, it is a straightforward task to calculate the filling time for this geometry, since its volume, the inlet area and inlet velocity are known; it turns out to be around 0.03 s. We can then calculate the time-averaged force over the core for the case with the outlet, using a time interval that is much greater than the filling time determined for the case without the outlet; in fact, 0.6 s was used, which implies that the steady-state value is being calculated, to all intents and purposes. The forces acting on the core can be due either to viscous shear or to the pressure; the latter turn out to be much greater than the former, and this is why we present only the latter for these 2D computations. In particular, we consider here the time-averaged force in the x -direction, \bar{F}_x ; its relation to the instantaneous force in the x -direction, F_x , and filling time, t_{fill} , is given in the appendix, which also contains formulae required later for forces in the y - and z -directions in the 3D computations.

The results for \bar{F}_x are shown in Figure 6. The $k-\varepsilon$ model gives an average value of 88 N, whereas the $k-\omega$ -SST and Spalart-Allmaras models give around 96 N and 98 N, respectively. The calculated value using the $k-\varepsilon$ model, however, differs from that determined by the $k-\omega$ -SST model by about 9% and from that determined by the Spalart-Allmaras model by more than 10%. On the basis of the standard deviation, it can be seen that \bar{F}_x as computed in the Spalart-Allmaras model is less variable compared to those in the other two turbulence models. This may, in part, be the consequence of their more detailed modelling of the

eddy viscosity, employing two equations instead of one for the Spalart-Allmaras model. It is, however, still important to note that the difference in time average of the pressure force on the salt core lies well within the interval constrained by the standard deviation.

Figure 6 Comparison of the effective mean pressure force in the x -direction when using different turbulence models



Note: The vertical bars show the standard deviation.

3.1.4 Comments on turbulence model comparison

On the basis of the investigations, it is not clear which turbulence model provides the optimal solution for the calculation of the eddy viscosity or the acting forces on the salt core during the filling process. Both the oneequation Spalart-Allmaras model, as well as the two twoequation models ($k-\epsilon$ and $k-\omega$ -SST), can be used for imaging the metal flow present in die casting.

On the other hand, the $k-\epsilon$ turbulence model deviates from the other two in the modelling of near-wall flow and the calculation of the effect of the force on the salt core. When calculating the pressure force $\bar{F}_{x,p}$ on the salt core, the results of the $k-\epsilon$ turbulence model are about 9–10% lower than those of the other turbulence models. In addition, the use of the $k-\epsilon$ turbulence model requires most computation time, followed by the $k-\omega$ -SST and Spalart-Allmaras models. The $k-\omega$ -SST model requires approximately 10% more computation time compared to the Spalart-Allmaras model. Further investigations (flow/metal jet behaviour and acting pressure force) give no indication which gives the more accurate solution. A corresponding validation of the results, in the form of practical trials or the use of other software packages (Flow-3D or similar), could provide additional information.

For further simulations and force calculations, the $k-\omega$ -SST model was used, in view of its extreme robustness (Robertson et al., 2015). In general, it is said to model separation areas and large pressure gradients very well and to provide good results both for wall-close as well as wall-free flow regions; all of these are necessary for an optimal mould filling simulation. Moreover, in our own experience, it proved to be the most stable in early exploratory runs, when the requirements for appropriate meshing were as yet unknown. Another reason for not selecting the Spalart-Allmaras turbulence model is its weakness in the

modelling of flow detachment and free shear layers (Spalart and Allmaras, 1994), such as occur during a filling process.

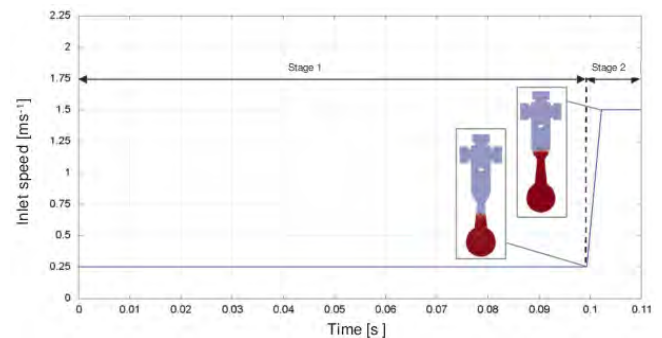
3.2 Mould filling in 3D

In this section, three-dimensional mould fill simulations are performed, both with OpenFOAM and the commercial simulation software MAGMA⁵, and assessed for plausibility. The three-dimensional flow geometry used for this purpose is shown in Figure 2. The turbulence model chosen was $k-\omega$ -SST, as this model is widely reported to be the most suitable for turbulence in flows that are dominated by wall shear stresses (Menter et al., 2003).

3.2.1 Casting curve and mesh

Figure 7 shows the speed curve considered, which consists of the first (dosing) and second (mould filling) stages of the filling process; note that the profile of the speed curve is ramped in this way because of the inertia of the shooting unit and the piston. The curve gives the course of the melt speed at the inlet, v_l . At the beginning of the filling simulation, the inlet speed is $v_l = 0.25 \text{ ms}^{-1}$ (stage 1). After a filling time of 99.4 ms, the casting piston accelerates within 2.8 ms to a speed of $v_l = 1.5 \text{ ms}^{-1}$ (stage 2). Immediately before acceleration, the melt flows in the runner and after the acceleration process to the gating, as seen in Figure 7. The shape is then filled with $v_l = 1.5 \text{ ms}^{-1}$. The (analytically) calculated melt speed at the gate is around 60 ms^{-1} .

Figure 7 The casting curve used for the 3D computations (see online version for colours)



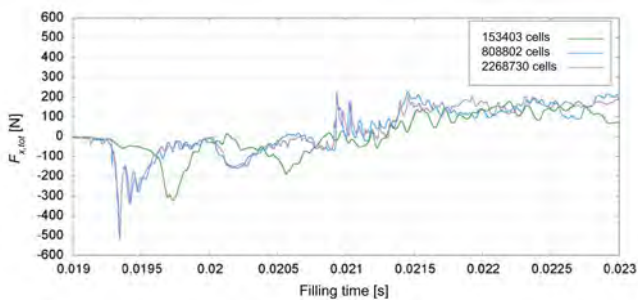
3.2.2 Influence of the mesh spacing

An unstructured mesh consisting of tetrahedra and a prism layer on the salt core was generated for the three-dimensional mould fill simulation using the commercial meshing tool ANSA (version 15.1.2). To test the influence of mesh spacing, three such meshes were used. The coarsest mesh consisted of 153403 cells, the cell size being between 1–4 mm edge length with the salt core being meshed with an edge length of 2 mm. The second mesh is composed of 808,802 cells whose edge length is in the range of 0.5 mm to about 2 mm, wherein the cell edge length varies between 0.5 mm (e.g. at salt core and gating) and about 2 mm (e.g. in the sprue and mould cavity). The

finest mesh consists of a total of 2,268,730 cells. The core was made with 0.2 mm edge length and the remaining flow area is from 0.2 mm to about 1.5 mm. For the investigation of the mesh influence, simulations were carried out with a constant inlet speed of $v_I = 1.5 \text{ ms}^{-1}$. The force profile is calculated from the time between 0.019 s and 0.023 s, which is the time interval during which the melt first hits the salt core.

Figure 8 shows the x-direction force component, $F_{x,tot}$, at the salt core as a function of mould filling time for the three meshes, and indicates that, for the coarsest mesh, the force profile on the salt core strongly deviates from that for the two finer meshes. This indicates a mesh independent result for the latter two meshes, although not for the former. Thus, in the present case, refining the mesh from 153,403 cells (net edge length at the core 2 mm) to 808,802 cells (net edge length at the core 0.5 mm) gives a more detailed resolution of the force at the core, although there is no advantage in further refinement to 2,268,730 cells (net edge length at the core 0.2 mm). Furthermore, since the computing time increases with the number of cells, the calculation of the force with the 808,802-cell mesh is the most suitable; in passing, we note that each run using this mesh required around 15 hours on the computational architecture named earlier.

Figure 8 Computed force component $F_{x,tot}$ on the salt core as a function of time for three different meshes (see online version for colours)



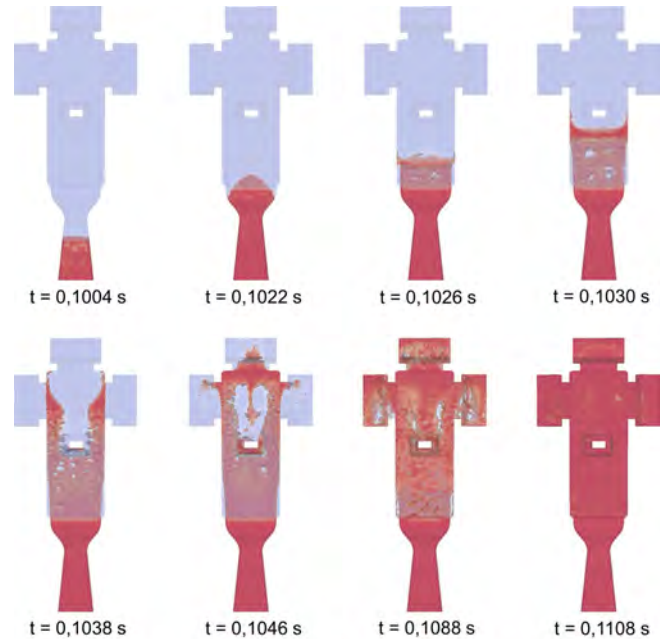
3.2.3 Simulation of the mould filling

In this section, the melt pattern simulated in OpenFOAM and visualised by ParaView is reproduced and discussed in the form of snapshots during threedimensional shape filling. The melt flow is shown in Figure 9.

On the basis of the simulation results, the mould filling begins with an initially slow and even melt advance in the sprue ($t = 0.1004 \text{ s}$), before the first inhomogeneities form in the melt front directly at the gate and at the inlet into the mould cavity ($t = 0.1022 \text{ s} / t = 0.1026 \text{ s}$). On entering the mould cavity, the liquid metal accumulates ($t = 0.1026 \text{ s}$), creating a wave at the front, which then hits the salt core ($t = 0.1030 \text{ s}$). The salt core disperses the melt into all spatial directions. At the same time, a large part of the melt flows past the salt core due to the wide cross section ($t = 0.1038 \text{ s}$). A proportion of melt is deflected to the sides by the salt core. The melt impinges on the opposite-facing wall, divides there and accumulates. Consequently, a melt

flow takes place, as a result of which the mould is completely filled in the sense of the return-flow filling ($t = 0.1088 \text{ s} / t = 0.1108 \text{ s}$). It can be observed here that, due to the symmetrical geometry, a dense, back-flowing melt current is generated which impinges on the rear side of the core ($t = 0.1046 \text{ s}$).

Figure 9 Time evolution of the melt flow in the mid-cross section during mould filling, as calculated using OpenFOAM (see online version for colours)



Notes: The areas in red indicate where $\gamma = 1$; the white area indicates the salt core. In all other areas, $\gamma < 1$.

The simulated metal flow or mould filling in the die casting process is quite realistic. As described in the literature (Nogowizin, 2010) and observed from the simulation results, a metal jet forms in the section due to the high melt speed, with the speed at the ingate, v_A , exceeding 60 ms^{-1} ; thus, the jet has a sufficiently high kinetic energy to reach the opposite-facing wall, at a distance of 100 mm, and then to flow back. Likewise, the centrifugal melt stream, which is produced by the combination of the flow components around the salt core on the wall, as shown in Figure 9 for $t = 0.1046 \text{ s}$, is typical of the filling of the mould with a central obstacle in the mould cavity.

Although jet splitting is minimally apparent from a distance of about 15 mm after the gate, the formation of individual pockets of melt could not be seen during the simulation. This difference is most probably due to the generated mesh, which in this case was too coarse to resolve the jet breakup precisely. Furthermore, it is assumed that the low kinetic energy of individual metal droplets does not negatively impact the salt core and thus their exact resolution plays a subordinate role for this simulation.

To assess the plausibility of the simulation results, analytically calculated and numerically determined form filling times were compared. Using the casting curve for v_I

defined in Figure 7, an analytically determined mould filling time, t_{an} , of 0.11092 s is calculated. This comes from noting that, for the geometry shown in Figures 2 and 3, the volume to be filled, V_{fill} , is $1.1 \times 10^5 \text{ mm}^3$, whereas the area of the inlet, A_I , is $2.7 \times 10^3 \text{ mm}^2$; hence, t_{an} is given by the solution to

$$V_{fill} = A_I \int_0^{t_{an}} v_I dt \quad (15)$$

which can be determined analytically because of the piecewise linear form of v_I . On the other hand, the simulated form filling gives a time of $t = 0.11089 \text{ s}$. Thus, these values are about 0.03% apart, whereby the results of the analytically and numerically calculated mould filling times are nearly identical. This comparison is a further indication of the realistic simulation results obtained with OpenFOAM.

3.2.4 Comparison of form filling with commercial software MAGMA⁵

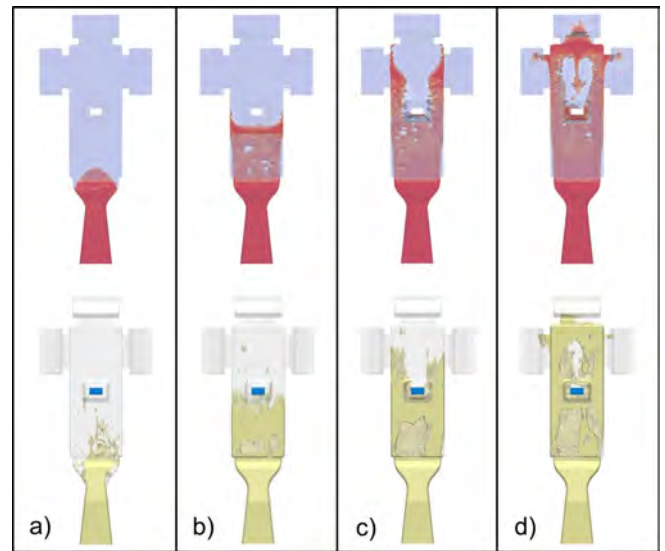
In addition to the form fill simulation using OpenFOAM, a simulation using the commercially available casting simulation software MAGMA⁵ was conducted. By comparison, in the form of snapshots of the filling process, it will be shown to what extent the simulation results obtained differ from one another and where the OpenFOAM solver exhibits strengths or weaknesses for the current application. As far as possible, identical simulation conditions are selected in MAGMA⁵, e.g. temperature, casting curve, material values, and so on. Due to the different workflow in MAGMA⁵, some parameters could not be kept the same. For example, the meshes in the simulation experiments differ from each other; the generated mesh in MAGMA⁵ has a cell edge length that is approximately 0.5 mm everywhere, and is therefore finer in the bulk than the mesh used for the OpenFOAM computations.

The simulation results of the two melt runs during the mould filling are compared in Figure 10. As can be seen, there are differences in the flow. This does not necessarily mean that one of the two is erroneous; indeed, in the modelling of high-pressure die casting, it is not uncommon for different software to give different results (Cleary et al., 2006; Ha et al., 1999, 2003). For example, when the melt enters the mould cavity, the atomising effect is more pronounced in the mould filling simulation with MAGMA⁵, as seen in Figures 10(a)–(c), although this is probably due to the differently generated mesh and the reduced cell spacing in MAGMA⁵. As melt filling proceeds, the interface in MAGMA⁵ becomes rougher, while the OpenFOAM simulation shows a smoother interface. However, as previously outlined, the droplets that are formed in the jet phase of the melt flow are of minor importance as regards the stresses on the salt core, as they carry less momentum than would be necessary to severely stress it.

Furthermore, for the mould filling simulation with MAGMA⁵, an interesting flow pattern occurs after the entry

of the melt into the mould. We see here partial recirculation of the inflowing melt along the walls of the die. This flow pattern is then advected further up the die as more melt flows in, as seen in Figure 10(b)–(d). For the mould fill simulation with OpenFOAM, there is different flow behaviour; here, a wave builds up, as seen in Figure 10(b), which is advected to the salt core or the opposite wall. This unequal flow behaviour may be once again due to the difference between the meshes, especially in the vicinity of the wall, and due to the different numerical solution algorithms which the two programs use. Because the exact numerical program settings in MAGMA⁵ are unknown to the user, no further clarification is possible.

Figure 10 Comparison of time evolution of the melt flow in the mid-cross section during mould filling, as calculated with OpenFOAM (upper row) and MAGMA⁵ (lower row), at four different times: (a) 0.1022 s (b) 0.1030 s (c) 0.1038 s (d) 0.1046 s (see online version for colours)



Another apparent difference between the simulations with MAGMA⁵ and OpenFOAM is the symmetric behaviour of the melt flow. While the computation with OpenFOAM gives a nearly symmetrical melt flow, the MAGMA⁵ solver gives an asymmetric melt flow, as seen in Figure 10(c). Since the performed form fill simulations are based on a symmetrical geometry, as shown in Figure 2, the solution with OpenFOAM is more plausible in this respect. Without further access to the MAGMA⁵ code, it remains unclear what would cause the asymmetric behaviour of the melt flow.

Overall, the mould filling simulations with MAGMA⁵ and OpenFOAM are both plausible, in spite of the fact that they are not identical. One disadvantage with OpenFOAM, as opposed to MAGMA⁵, is the required computing time, which is more than five times greater. However, the MAGMA⁵ user, in contrast to the OpenFOAM user, no access to the numeric program settings and source codes, so that a case adaptation or programmer extension with MAGMA⁵ is not possible. MAGMA⁵ also does not allow the forces acting on the salt core during the filling process to

be written out and hence no statements regarding the core failure are possible. With OpenFOAM, interventions in the solution algorithm or force calculations on the salt cores are possible, and hence the use of OpenFOAM for this type of simulation is more advantageous for the particular field of interest.

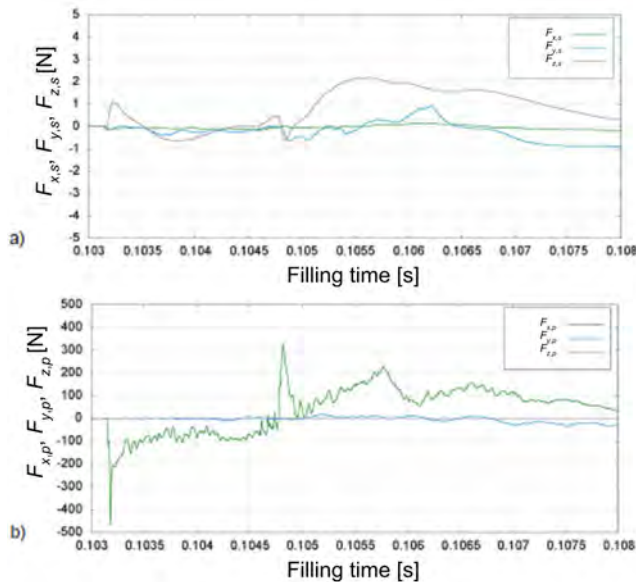
3.3 Investigation of the forces acting on the salt core

During the flow of the melt around the salt core, the surface force, which is composed of shear and pressure forces, may cause the failure of the salt core. In order to understand this better, the following section will explain and describe the forces and their components in more detail. This can be done in OpenFOAM using the function object called *forces*. We start by explaining the different components of the forces.

3.3.1 Pressure and shear forces

Since the load on the salt cores due to the air flow in the mould cavity is negligible, the forces will be considered starting from the time of impact of the melt on the core. The evaluation of the forces takes place during the filling of the mould in the range of 0.103 s to 0.108 s. The melt-induced forces are shown in Figure 11.

Figure 11 (a) Shear forces in x -, y - and z -directions (b) Pressure forces in x -, y - and z -directions (see online version for colours)



The inhomogeneous, fluctuating lines of the individual force components show that the core is exposed to strong dynamic stresses during the filling process. This behaviour results from the eddies and vortices in the melt during the filling of the mould. Furthermore, it can be seen from the force profile that both the shear forces in Figure 11(a) in the x -, y - and z -directions with a maximum value of 2.2 N, as well as the pressure forces in Figure 11(b) in the y - and z -directions with a maximum of approximately 30 N, are significantly lower than the pressure force in the x -direction.

The pressure force acting in the x -direction has a maximum value of approximately 500 N and is thus over 200-fold or 15 times higher than the other five force components. Thus, the shear force components, as well as the pressure force components acting in the y - and z -directions, would be expected to play a negligible role in any possible salt core collapse. The shear forces can only contribute to the removal of single particles/grains from the salt core surface and the stability of the salt core. The pressure force in the x -direction is, in this case, the failure-critical force component. The high pressure force, F_x , is caused by the nearly orthogonal impact of the melt-air interface in the x -direction during the filling process. Note that the depicted negative values for the force in Figure 11 result from the definition of the Cartesian coordinate system; thus, negative values mean the resulting pressure force component, and the positive value of F_x depicted in Figure 11 is due to the back flow on the opposite face of the salt core.

As already described, the force component acting on a rectangular cross-section in the flow direction is almost solely due to the pressure. Since it is transversely directed at the rectangular salt core in this simulation case, the force profile shown is conclusive. The highest value for $F_{x,p}$ was obtained at the first contact of the melt with the core and is about 470 N. Thus, this is the time that is most critical for the salt core. The forces following this first moment of impact are lower by a factor of between 2 and 3 and are therefore not as critical. However, since Fuchs et al. (2013) reported a significant decrease in core strength if temperature is involved, these forces may also be of importance if the heat from the inflowing melt is transferred quickly enough to the core, causing its strength to deteriorate. This may perhaps be investigated in future work.

3.3.2 Influence of the flow velocity on the forces

The speed of the melt during mould filling is a significant quantity for the extent of the force on the salt core. To investigate the speed's influence for the present case, constant inlet velocities (piston speeds) in the range of $v_l = 0.5 - 1.5 \text{ ms}^{-1}$ at intervals of 0.25 ms^{-1} were defined as boundary conditions and simulated. All other boundary conditions are the same for all simulations. The grid was also the same as for previous 3D calculations, i.e., 808,802 cells with an edge length in the range 0.5–2 mm.

Figure 12 shows the results obtained for $F_{x,tot}$, as defined in equation (A.1), during mould fill simulation for different inlet speeds. It can be seen from the curves that the pressure force increases with increasing inlet or piston speed. For a piston speed of 0.5 ms^{-1} , which corresponds to $v_A \approx 20 \text{ ms}^{-1}$, a maximum force of $F_{x,tot} = 5 \text{ N}$ acts on the core; for a piston speed of 1.5 ms^{-1} , corresponding to $v_A \approx 60 \text{ ms}^{-1}$, $F_{x,tot}$ can exceed 500 N.

3.3.3 Core viability

Given the computed resulting force plotted in Figure 12, it is now of interest for the design engineer to feed this into a

solid model to see how the loads compare to the strength of the salt core. Since the jet melt is impinging more or less in the middle of the core and the core so closely resembles a simple beam, Euler-Bernoulli beam theory can be applied in the context of a three-point bending test. According to the formula, which can, for example, be found in Beitz et al. (2013), the resulting bending stress, σ_b , in a beam oriented as shown in Figure 2, i.e., extending in the z -direction and the force impacting in the negative x -direction, can be calculated according to

$$\sigma_b = \frac{M_b \cdot h}{SI_x} \quad (16)$$

where M_b is the bending moment, I is the second moment of area or moment of inertia of plane area and h is the extent of the beam in the x -direction. For the configuration shown in Figure 2, the second moment of area is calculated as (Beitz et al., 2013)

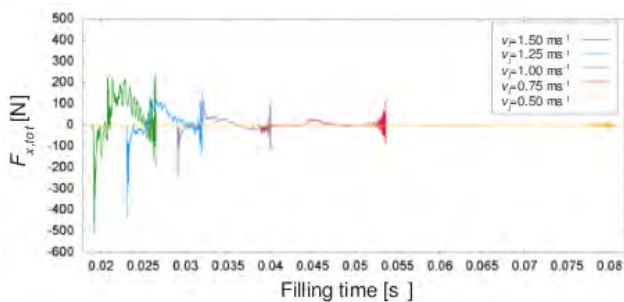
$$I_x = \frac{bh^3}{12} \quad (17)$$

where b is the extent of the beam in the y -direction; thus, we have $b = 10$ mm and $h = 5$ mm. It follows from equation (16) that x as the direction of the impacting force vector has to be put in as the outermost distance of the beam in the x -direction to calculate the maximum bending stress. The material property bending strength has been previously reported for the salt core material in literature (Fuchs et al., 2013; Yaokawa et al., 2006; Yamada, 2013). The bending moment itself can be calculated from the resulting force impacting in the centre of the beam, also by a simple formula according to Beitz et al. (2013),

$$M_b = \frac{F \cdot Z}{4} \quad (18)$$

With Z being the length of the beam outside the bearing. According to this definition and Figure 2, $Z = 70$ mm was inserted into equation (18) to obtain the values together with the maximum force, F_x^{\max} , taken from Figure 12. Doing those simple calculations yields the bending stress values according to Table 2.

Figure 12 Computed force component $F_{x,tot}$ on the salt core as a function of time for five different inlet speeds, v_I (see online version for colours)



The values in Table 2 are also further supported by a FEM study that led to the same result using a module in the CAD

software CATIA. It is now possible to match the results with the strength values available in literature. Here, one has to be careful regarding the process that is used for manufacturing the salt cores. While Fuchs et al. (2013) tested pressed salt cores and report strength of about 13 MPa, Yaokawa et al. (2006) and Yamada (2013) reported strengths up to 42 MPa for cast salt cores manufactured with the correct parameters, with the superheat of the salt melt as the most sensitive one. The common ground among those sources is that, in both cases, a core would crack for the three highest ingate velocities (40, 50 and 60 ms^{-1}), while it would hold for ingate velocities of 20 and 30 ms^{-1} . However, the reader should bear in mind that those values are valid only for the tested geometry, as the velocity values at the core are the failure critical ones. These simple calculations, however, clearly underscore the diminishing importance of the difference caused by the different treatments of the turbulence as discussed earlier. They account for differences in forces only by at most 10%. It also resembles the findings of Fuchs et al. (2013) that the velocity is the most critical parameter for core failure. Furthermore, it also indicates that the presented model is crucially important in allowing the engineer to design process parameters, as the actual stresses the core has to bear will sensitively depend on the actual geometry. This emphasises the appropriateness of the CFD approach, which can account for different shapes. The parameter set where the process leads to sound castings with intact cores will always be different depending on the shape.

Table 2 Bending stresses for the evaluated ingate velocities

v_I/ms^{-1}	v_A/ms^{-1}	F_x^{\max} / N	σ_b/MPa
0.5	20	5	2.1
0.75	30	30	12.6
1.0	40	250	105
1.25	50	450	189
1.5	60	500	210

4 Conclusions

The research work explained throughout the course of this paper shows that it is possible, even with freely available open-source software, to conduct a reasonable prediction of the forces on lost cores involved during the filling process in HPDC. The displayed results are in agreement with previously published data and conclusions (Fuchs et al., 2013; Fuchs and Körner, 2014), and the results of the presented model allow the CAD-design engineer to evaluate *a priori* whether an envisaged core, die and parameter design will withstand the stresses during casting processing. Moreover, the main focus of this study was to evaluate how carefully the particular turbulence model needs to be selected. The academic discussion in this field is quite comprehensive and the differences and different sustainability of particular turbulence models have been pointed out at numerous times since academic papers were

written on turbulence models using the RANS-approach. However, this academic discussion about the significance of the different turbulence models does not seem to be in line with this application-oriented study. Even though we benchmarked two turbulence models that are of inferior capabilities for the problem at hand ($k-\varepsilon$ and Spalart-Allmaras) with one that has collected much academic acclaim for this kind of flow situation ($k-\omega$ -SST), the differences do not practically matter. In particular, the difference between the Spalart-Allmaras model and the $k-\omega$ -SST model do not seem to be as pronounced as one would expect, given the academic opinion that the Spalart-Allmaras model due to its high reliance on empirical parameters is only suitable for external aerodynamic applications. Contradictory to this opinion, the displayed results show that this difference is of negligible order of magnitude for this field of application.

On the other hand, it is much more important to design the casting, die and, as pointed out, process parameters very carefully. It will be the momentum of the melt impacting the core that determines the order of magnitude of the force acting on it and thus its likelihood of viability. The viability of the core will in turn determine whether the process leads to sound castings.

Lastly, from a CFD perspective, we may note that this is the first time that OpenFOAM has been employed for the modelling of high-pressure die casting, constituting a new field of application for this rapidly growing software (Robertson et al., 2015).

References

- Beitz, W., Küttner, K.H. and Davies, B.J. (2013) *DUBBEL – Handbook of Mechanical Engineering*, Springer-Verlag London.
- Brackbill, J.U., Kothe, D.B. and Zemach, C. (1992) 'A continuum method for modeling surface tension', *Journal of Computational Physics*, Vol. 100, No. 2, pp.335–354.
- Cleary, P.W., Ha, J., Prakash, M. and Nguyen, T. (2006) '3D SPH flow predictions and validation for high pressure die casting of automotive components', *Applied Mathematical Modelling*, Vol. 30, No. 11, pp.1406–1427.
- Courant, R., Friedrichs, K. and Lewy, H. (1967) 'On the partial difference equations of mathematical physics', *IBM Journal of Research and Development*, Vol. 11, No. 2, pp.215–234.
- Ferrer, P.J.M., Causon, D.M., Qian, L., Mingham, C.G. and Ma, Z.H. (2016) 'A multi-region coupling scheme for compressible and incompressible flow solvers for two-phase flow in a numerical wave tank', *Computers and Fluids*, Vol. 125, pp.116–129.
- Fuchs, B., Eibisch, H. and Körner, C. (2013) 'Core viability simulation for salt core technology in high pressure die casting', *International Journal of Metalcasting*, Vol. 7, No. 3, pp.39–45.
- Fuchs, B. and Körner, C. (2014) 'Mesh resolution consideration for the viability prediction of lost salt cores in the high pressure die casting process', *Progress in Computational Fluid Dynamics*, Vol. 14, No. 1, pp.24–30.
- Ha, J., Cleary, P.W., Alguine, V. and Nguyen, T. (1999) 'Simulation of die filling in gravity die casting using SPH and MAGMASoft', *Proceedings of the 2nd International Conference on CFD in Minerals and Process Industries*, Melbourne, Australia, pp.423–428.
- Ha, J., Cleary, P.W., Prakash, M., Alguine, V., Nguyen, T. and Scott, C. (2003) 'SPH, MAGMASoft and water analogue modellings of die filling of a servo piston', *Proceedings of the 2nd International Conference on CFD in Minerals and Process Industries*, Melbourne, Australia, pp.587–592.
- Hirt, C.W. and Nichols, B.D. (1981) 'Volume of fluid (VOF) method for the dynamics of free boundaries', *Journal of Computational Physics*, Vol. 39, No. 1, pp.201–225.
- Jasak, H., Jemcov, A. and Tuković, Z. (2007) 'OpenFOAM: a C++ Library for Complex Physics Simulations', Paper presented at the *International Workshop on Coupled Methods in Numerical Dynamics IUC*, Dubrovnik, Croatia, 19–21 September, 20pp.
- Jelínek, P. and Adámková, E. (2014) 'Lost cores for high-pressure die casting', *Archives of Foundry Engineering*, Vol. 14, No. 2, pp.101–104.
- Koch, M., Lechner, C., Reuter, F., Köhler, K., Mettin, R. and Lauterborn, W. (2016) 'Numerical modeling of laser generated cavitation bubbles with the finite volume and volume of fluid method, using OpenFOAM', *Computers and Fluids*, Vol. 126, pp.71–90.
- Launder, B.E. and Spalding, D.B. (1974) 'The numerical computation of turbulent flows', *Computer Methods in Applied Mechanics and Engineering*, Vol. 3, pp.269–289.
- Mayon, R., Sabeur, Z., Tan, M-Y. and Djidjeli, K. (2016) 'Free surface flow and wave impact at complex solid structures', Paper presented at the *12th International Conference on Hydrodynamics*, Egmond aan Zee, NL, 18–23 September, Paper ID: 154, 10pp.
- Menter, F.R. (1994) '2-equation eddy-viscosity turbulence models for engineering applications', *AIAA Journal*, Vol. 32, No. 8, pp.1598–1605.
- Menter, F.R., Kuntz, M. and Langtry, R. (2003) 'Ten years of industrial experience with the SST turbulence model', *Turbulence, Heat and Mass Transfer*, Vol. 4, pp.625–632.
- Nogowizin, B. (2010) *Theorie und Praxis des Druckgusses*, Fachverlag Schiele & Schön.
- Robertson, E., Choudhury, V., Bhushan, S. and Walters, D.K. (2015) 'Validation of OpenFOAM numerical methods and turbulence models for incompressible bluff body flows', *Comp. Fluids*, Vol. 123, pp.122–145.
- Spalart, P.R. and Allmaras, S.R. (1994) 'A one-equation turbulence model for aerodynamic flows', *Recherche Aerospaciale*, No. 1, pp.5–21.
- Versteeg, H. and Malalasekera, W. (2007) *An Introduction to Computational Fluid Dynamics: The Finite Volume Method*, 2nd ed., Pearson.
- Weller, H.G., Tabor, G., Jasak, H. and Fureby, C. (1998) 'A tensorial approach to computational continuum mechanics using object-oriented techniques', *Computers in Physics*, Vol. 12, No. 12, pp.620–631.
- White, F.M. (2011) *Fluid Mechanics*, 7th ed., McGraw-Hill, New York.
- Wilcox, D.C. (1988) 'Reassessment of the scale determining equation for advanced turbulence models', *AIAA Journal*, Vol. 26, No. 11, pp.1299–1310.

Yakhot, V., Orszag, S.A., Thangam, S., Gatski, T.B. and Speziale, C.G. (1992) 'Development of turbulence models for shear flows by a double expansion technique', *Physics of Fluids A: Fluid Dynamics*, Vol. 4, pp.1510–1520.

Yamada, Y. (2013) EP Patent No. 20090742774 (July 10, 2013)

Yaokawa, J., Miura, D., Anzai, K., Yamada, Y. and Yoshii, H. (2006) 'Mechanical properties of salt core comprised of alkali carbonate and alkali chloride', *Journal of Japan Foundry Engineering Society*, Vol. 78, pp.1510–1520.

Appendix

For $i = x, y, z$, the total force acting on the core in direction i , $F_{i,tot}$, is given by

$$F_{i,tot} = F_{i,p} + F_{i,s} \quad (\text{A.1})$$

where $F_{i,p}$ and $F_{i,s}$ are pressure and viscous shear forces, respectively, and are given by

$$F_{i,p} = - \iint_{A_c} p n_i dA \quad (\text{A.2})$$

$$F_{i,s} = \iint_{A_c} (\mu + \mu_{tur}) \left(\frac{\partial U_i}{\partial x_j} + \frac{\partial U_j}{\partial x_i} \right) n_j dA \quad (\text{A.3})$$

where $\mathbf{U} = (U_x, U_y, U_z)$ and A_c is the surface area of the core.

Thence, the average pressure and viscous forces, $\bar{F}_{i,p}$ and $\bar{F}_{i,s}$ respectively, over a filling time t_{fill} are given by

$$\bar{F}_{i,p} = \frac{1}{t_{fill}} \int_0^{t_{fill}} F_{i,p} dt, \quad \bar{F}_{i,s} = \frac{1}{t_{fill}} \int_0^{t_{fill}} F_{i,s} dt \quad (\text{A.4})$$